ACS NANO

www.acsnano.org

ARTICLE

Photon-Momentum-Enabled Electronic Raman Scattering in Silicon Glass

Sergey S. Kharintsev,* Elina I. Battalova, Aleksey I. Noskov, Jovany Merham, Eric O. Potma, and Dmitry A. Fishman*

Cite This: *ACS Nano* 2024, 18, 9557−9565

Read Online

ACCESS | Metrics & More | Article Recommendations | Supporting Information

ABSTRACT: **The nature of enhanced photoemission in disordered and amorphous solids is an intriguing question. A point in case is light emission in porous and nanostructured silicon, a phenomenon that is still not fully understood. In this work, we study structural photoemission in heterogeneous cross-linked silicon glass, a material that represents an intermediate state between the amorphous and crystalline phases, characterized by a narrow distribution of structure sizes. This model system shows a clear dependence of photoemission on size and disorder across a broad range of energies. While phonon-assisted indirect optical transitions are insufficient to describe observable emissions, our experiments suggest these can be understood through electronic Raman scattering instead. This phenomenon, which is not commonly observed in crystalline semiconductors, is driven by structural disorder. We attribute photoemission in this disordered system to the presence of an excess electron density of states within the forbidden gap (Urbach bridge) where electrons occupy trapped states. Transitions from gap states to the conduction band are facilitated through electron−photon momentum matching, which resembles Compton scattering but is observed for visible light and driven by the enhanced momentum of a photon confined within the nanostructured domains. We interpret the light emission in structured silicon glass as resulting from electronic Raman scattering. These findings emphasize the role of photon momentum in the optical response of solids that display disorder on the nanoscale.**

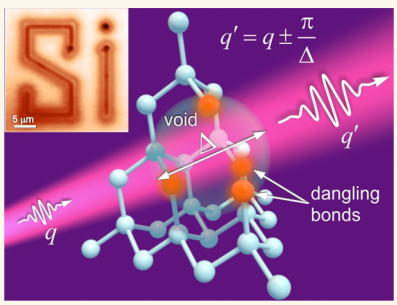

KEYWORDS: *semiconductor glass, electronic Raman scattering, Compton scattering, Urbach bridge, photon momentum, structural optical spectroscopy*

INTRODUCTION

Light absorption and emission in indirect bandgap materials is of keen interest in photovoltaics and optoelectronics.[1,2] Silicon is a case in point, as it lies at the heart of modern electronics.[3] An important challenge in photonics is to forge direct absorption and emission channels in Si throughout the visible and near-infrared range.[4,5] Tunable visible photoluminescence (PL) in porous silicon (p-Si) emerged in the early 1990s and presented exciting prospects for light-emitting silicon devices.[6−10] Nonetheless, despite impressive advances ever since, the origin of PL in Si remains a subject of debate.

Quantum confinement effects, as pioneered by Canham, have been suggested as a possible explanation for the PL phenomenon.[4,11] The confinement model offers mechanisms for light emission in different forms of structured silicon, including indirect radiative recombination of excitons localized in crystalline silicon (c-Si) quantum dots,[12−14] radiative recombination of electron−hole pairs trapped at surface states of p-Si,[15] and light emission from chemical impurities anchored to the structural defects and asperities of p-Si.[7,16−18] All aforementioned emission mechanisms indicate an increase of the local electronic density of states (e-DOS) at nano- and sub-nanostructures, which include defects, dangling bonds, and chemical moieties.[19,20] Unfortunately, these models fall short in elucidating the anomalous PL redshift observed in Si nanocrystals.[21,22]

Our study delves into the photoemission of a heterogeneous cross-linked Si glass produced by continuous wave (cw) laser annealing of amorphous silicon (a-Si). The glass comprises crystalline Si nanoclusters cross-linked to an amorphous matrix. Upon illumination with cw radiation, the glass emits two distinct bands, previously denoted as low-energy PL (band S) and high-energy PL (band F),[6] whose origins have remained unclear. Here, we suggest that both emission bands originate from electronic Raman scattering (ERS).[23−27]

Received: December 15, 2023
Revised: February 17, 2024
Accepted: February 29, 2024
Published: March 4, 2024

https://doi.org/10.1021/acsnano.3c12666
ACS Nano 2024, 18, 9557−9565

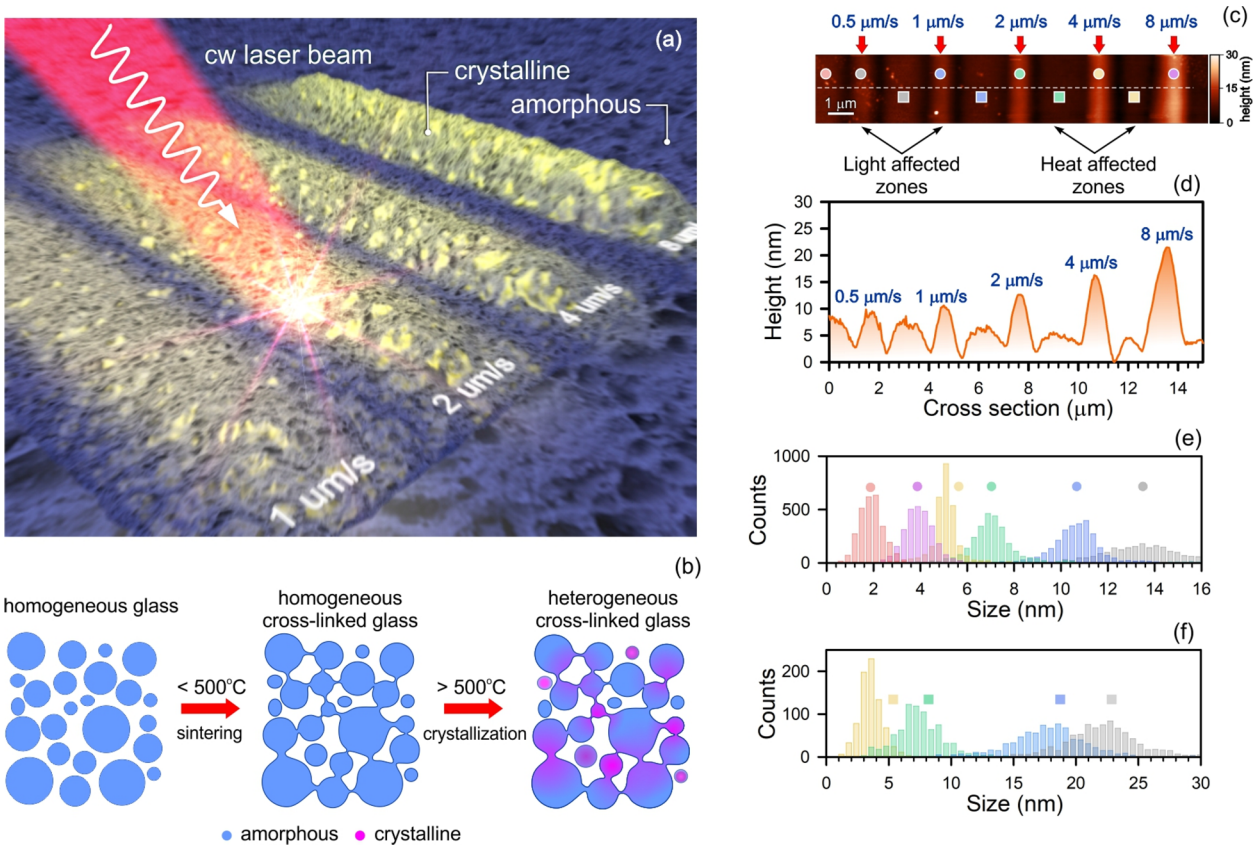

Figure 1. (a) An artistic representation of light-assisted formation of cross-linked semiconductor glass stripes on an a-Si film. (b) Schematic representation of temperature-dependent formation of homogeneous cross-linked glass (through sintering) and heterogeneous cross-linked glass (through crystallization). (c) AFM topography and (d) cross-section of an array series. By varying exposure time (writing speed), one can form areas with different degrees of crystallinity and a narrow distribution of sizes (measured by their heights) within light affected zones (e) and heat-only affected zones (f).

One of the first observations of ERS in semiconductors has been linked to direct optical transitions between a light-hole band and a heavy-hole band, an effect distinct from vibrational Raman scattering (VRS) where the initial and final electronic states remain identical.[25,26] We attribute the observed emission to ERS transitions from states within the bandgap, which, in the context of the Mott−Davis model for disordered semiconductors,[28,29] are expected to be present in the cross-linked silicon glass studied here. Because such Urbach states constitute trapped states for the electron, transitions in the proximity of the conduction band require a source of momentum. Although lattice phonons have been proposed to supply the necessary momentum, higher-energy transitions from deep trapped states would require the involvement of multiple phonons,[30] thus severely limiting the probability of such transitions. We propose that transitions from these states are enabled instead by electron−photon momentum matching, a result of quantum confinement,[31] particularly in a disordered medium. In this context, the momentum disparity between two electronic states is facilitated by the increased momentum distribution of the confined photon.

The concept of expanded near-field photon momentum has previously been proposed as a plausible explanation for enhanced interband two-photon excitation[32] as well as intraband transitions in gold nanostructures.[33] More recently, momentum expansion in plasmonic two-dimensional systems has been discussed, focusing on multipolar, spin-flip, and multiquanta emission processes.[34] Here we suggest that the existence of near-field photon modes with expanded momenta in a Si glass provides the necessary momentum to facilitate ERS transitions from trapped states in the bandgap. This effect is similar to Compton scattering, though with visible light photons.

In the context of disordered semiconductors, we revisit an idea proposed and developed by Mott and Davis[29,35] and use it to explain the PL phenomenon. The model is based on the concept of dangling bonds at vacancies, divacancies, or nanovoids. It introduces an excess electronic density of states within the forbidden gap,[36] forming an Urbach bridge of electronic states across the semiconductor bandgap. This bridge enables new electronic Raman transitions, including low-energy intraband transitions near the Fermi level (*l*-ERS), higher energy interband transitions in the extended tail near the conduction band (*h*-ERS), and optical transitions from deep states within the Urbach bridge (heavy tail transitions).

These emissions exhibit a strong correlation with structural size, a relationship that can be explained through the concept of electron−photon momentum matching. Given the direct link between optical signals and the formation of cross-linked semiconductor glasses, the findings presented here allow for the expansion of conventional optical spectroscopy for both chemical (energy) and structural (momentum) studies of disordered solids.

https://doi.org/10.1021/acsnano.3c12666
ACS Nano 2024, 18, 9557−9565

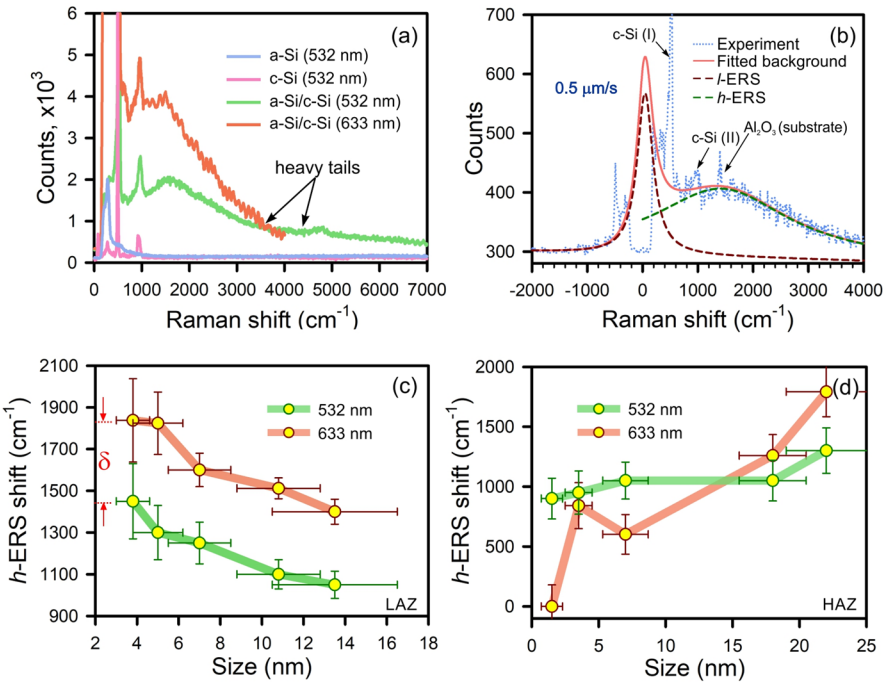

Figure 2. (a) Raman spectra of a-Si (light blue: exposure 10 s, intensity 0.4 MW/cm^2) and c-Si (pink: exposure 0.1 s, intensity 0.4 MW/cm^2) using 532 nm excitation and silicon glass at LAZ (8 μm/s) using 532 nm (green: exposure 10 s, intensity 0.4 MW/cm^2) and 633 nm (orange: exposure 10 s, intensity 1.5 MW/cm^2) excitation wavelengths. Camera sensitivity drops rapidly above 900 nm, i.e., at energy shift >4000 cm^{-1} for 633 nm excitation. (b) Decomposition of the Raman spectrum at LAZ written at 0.5 μm/s measured using the 633 nm excitation wavelength. (c and d) The *h*-ERS shift vs size for LAZ and HAZ using 532 and 633 nm excitation wavelengths.

RESULTS/DISCUSSION

First, we offer a strategy to produce samples where both crystallinity and structure size are known and formed in a controlled fashion. We consider a bottom-to-top approach, i.e., from a disordered state to a more ordered material state, by which amorphous silicon (a-Si) transforms in part into crystalline silicon (c-Si) through light-assisted thermal impact. This approach allows efficient photon absorption in an amorphous matrix followed by light emission at c-Si nanocrystal inclusions. To accomplish this, we deposit a 300 nm thick a-Si film on glass using chemical vapor deposition (see Methods/Experimental section). The film is then subjected to a tightly focused cw laser beam, which is scanned to write an array of straight lines at different scanning speeds (Figure 1a). The high light absorption (α = 83,870 cm^{-1} at 633 nm[37]) and low thermal conductivity (κ = 1.7−2.2 W/mK[38]) of a-Si give rise to local heating. In areas where light-induced temperature changes do not exceed 500 °C, this procedure results in the sintering of amorphous structures forming a homogeneous cross-linked glass (Figure 1b).[39,40] In areas where the temperature exceeds 500 °C, an amorphous-to-crystalline phase transition occurs, and a heterogeneous cross-linked semiconductor glass is formed. The resulting film, "foamed" by light, represents a heterogeneous disordered matrix in which electronic, optical, and thermal properties vary on the nanometer scale.

In our experiment, the local degree of crystallinity is determined by the speed of the scanning laser beam with an intensity of 2.5 MW/cm^2, which was set to 0.5, 1, 2, 4, or 8 μm/s. An AFM topography map in Figure 1c shows that an array of stripes can be easily formed, where their height increases proportionally with the scanning rate, reaching a few tens of nanometers. The leftmost distribution in Figure 1c and d corresponds to the intact a-Si region, providing a reference point. For intensities above 3 MW/cm^2, we observe the formation of bubbles on the surface of the film (see Supporting Information Part I, Figure SF1). These bubbles are prone to bursting, leading to the formation of significant protrusion areas that were used to assess the thickness of the initial a-Si film. Within the formed glass surface, we identified two distinct areas. The first is the light-affected zone (LAZ), which represents the area directly exposed to laser radiation. The second is the heat-only affected zone (HAZ), which encompasses the portion that remained unexposed to the laser and was solely influenced by the diffusion of heat.

Figure 1d shows structural growth within the LAZ. Changes in the film topology are caused by a more compact arrangement of atomic Si upon crystallization, leading to relaxation of intrinsic local stress to minimize the Gibbs energy. Here, we come across a counterintuitive observation: extended exposure times result in inferior crystallization and smaller structural formation. These can be explained by the larger thermal conductivity of c-Si ($\kappa_{c\text{-}Si}$ = 147 W/mK) compared to that of a-Si ($\kappa_{a\text{-}Si}$ = 1.7−2.2 W/mK). For this process, a negative feedback loop is initiated, causing crystallization to cease as a result of efficient heat transfer. The local temperature may drop below the threshold of 500 °C, while the film morphology continues to change due to sintering (Figure 1e).

The dissipation of heat beyond the LAZ induces changes in morphology and structure formation in the HAZ. Figure 1f illustrates a broader distribution of surface roughness in HAZ compared to that in LAZ. It can be seen that HAZ differs from LAZ by the lack of a crystalline (c-Si) phase. The degree of crystallinity in each zone is monitored using vibrational Raman scattering (VRS) microscopy.[24] While LAZ is clearly rich in c-

https://doi.org/10.1021/acsnano.3c12666
ACS Nano 2024, 18, 9557−9565

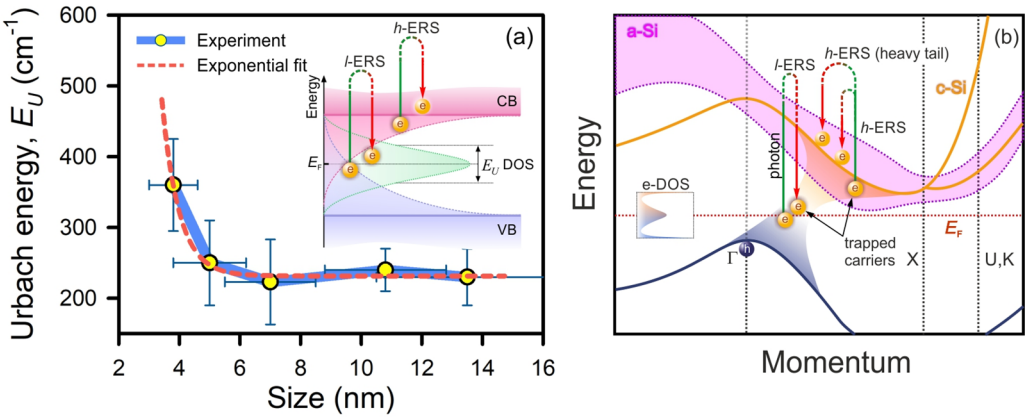

Figure 3. (a) The *l*-ERS line width at LAZ (Urbach energy) as a function of structure size. The inset shows a schematic representation of the Urbach bridge following the concept idea by Mott and Davis.[29,35] (b) Conceptual visual representation of direct and indirect optical transitions for understanding the origins of *l*-ERS and *h*-ERS.

Si, the temperature in HAZ does not exceed the required threshold. Meanwhile, crystallization in HAZ can be triggered by pressure and local stress[41] at amorphous/crystalline interfaces, an effect that is observed in our experiments near the zone boundaries (Figure 1f). In summary, laser writing yields a narrow distribution of nanostructure sizes within both LAZ and HAZ, as estimated from the surface roughness. This model system proves invaluable for exploring structure- and phase-dependent photoemission.

The Raman spectrum of LAZ, obtained at a position at which a writing speed of 0.5 μm/s was applied, is shown in Figure 2a. A rich emission spectrum covering a broad energy range is observed, where the presence of a crystalline phase can be inferred from the lines at 521 and 960 cm^{-1}, attributed to the first- and second-order (optical) phonon modes of c-Si.[42] The broad emission band, extending well beyond 5000 cm^{-1}, peaks near 1700 cm^{-1} for either the 532 or 633 nm excitation wavelength. The overall invariance of the emission maximum energy shift (or spectrum's center of mass) with respect to excitation wavelength is a signature of Raman scattering rather than luminescence resulting from the radiative recombination of thermalized electron populations in the conduction band with holes in the valence band. In addition, the observation of the emission at large Stokes shifts (>3000 cm^{-1}), which we refer to as the *heavy tail*, cannot be accounted for in the context of thermalization of electrons and holes (Supporting Information Part II, Figure SF2). Phonons are required for the thermalization process, yet the vibrational density of states (v-DOS) of the phonon bath is expected to be reduced for nanoscale structures, which can prolong the duration of thermalization by an order of magnitude.[22,43] The v-DOS becomes negligible for structures smaller than a few nanometers, so that the probability of emitting or absorbing phonons, needed for electron thermalization and indirect phonon-assisted transitions, is significantly reduced. Moreover, quantum confinement should raise the bottom edge of the conduction band at the Γ−X point of the Brillouin zone by 1 eV (Figure SF3). This means that the 633 nm photon carries insufficient energy to induce indirect interband transitions in such sub-nanometer structures. These considerations are at odds with a model that relies on emission from radiative electron−hole recombination, extensively discussed in Supporting Information Part II but comply with the ERS model for emission.

Figure 2b displays the full LAZ emission spectrum, showing spectral features on both the Stokes and anti-Stokes sides. In the following, we ignore the optical phonon signatures and focus solely on the broader spectral features. Using a regularized least-squares method, we decompose the spectral response into two distinct Lorentzian bands denoted as *l*-ERS (low-energy ERS near Fermi level, red dotted line, Figure 2b) and *h*-ERS (high energy shifted ERS band, green-dotted line, Figure 2b). We note that both *l*-ERS and *h*-ERS are absent in bulk c-Si; they only appear after the light-induced structuring in the a-Si material.

Figure 2c presents the central energy shift of *h*-ERS as a function of structural size using an excitation wavelength of either 633 or 532 nm (depicted by the blue solid curves). These plots reveal a clear trend: a pronounced redshift of *h*-ERS as the structure size is decreased. Below, we argue that this observation provides evidence for ERS from trapped states in nanocrystalline inclusions in the a-Si matrix (see also Figure SF5 and discussion therein). We observe an opposite trend for the size dependence of the *h*-ERS energy shift in HAZ. Figure 2d shows a blueshift as the structure size increases, which is observed for both excitation wavelengths. This latter phenomenon can be explained in the context of an amorphous semiconductor, which constitutes the only component in HAZ. In amorphous Si the energy band structure is smeared compared to the crystalline phase, associated with a decreasing bandgap when the structure size increases.[44,45] In the case of unperturbed a-Si with an ∼2 nm surface roughness, the *h*-ERS fully overlaps with *l*-ERS (see Supporting Information Part IV and Figure SF4). As the a-Si film is subjected to heat, its roughness increases due to the sintering process, leading to a redshift in the *h*-ERS, a result of size-dependent band smearing.

To explain the size-dependent emission energy shift in LAZ, we propose an alternative explanation for the emission origin in cross-linked semiconductor Si glasses that is based on ERS. In contrast to vibrational Raman scattering, ERS involves different initial and final *electronic* states in the material.[25,26] In the case of a localized photon, the change in electron momentum can be due to the interaction with a confined photon with an expanded momentum distribution, as depicted in Figure 3a.[23,24] Our model considers that, in disordered semiconductors, localized electron states form an increased electronic density of states (e-DOS) across the forbidden gap,

https://doi.org/10.1021/acsnano.3c12666
ACS Nano 2024, 18, 9557−9565

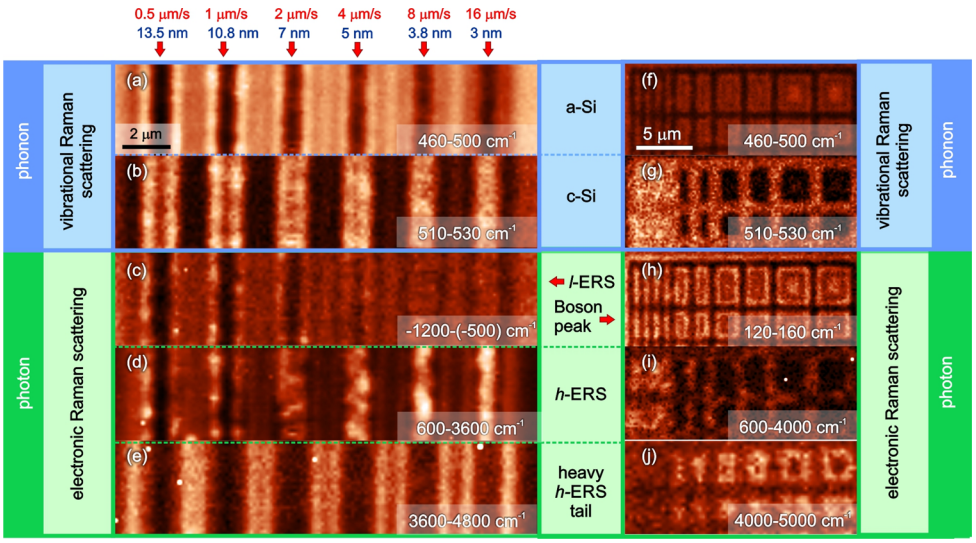

Figure 4. A 1D array of straight lines fabricated on a-Si film by using different laser scanning speeds: VRS maps (a-Si (a) and c-Si (b)) and ERS maps (*l*-ERS (c) and *h*-ERS (d, e)). A light-structured cross-linked network on a-Si film at different pitch: VRS maps (a-Si (f), c-Si (g), and a boson peak (h)) and ERS maps (*h*-ERS (i, j)).

extending from the band edges down to the Fermi level (Figure 3b and inset of Figure 3a), as was predicted by Mott et al.[29,35] Molecular dynamics simulations reveal that defect-induced Hellman−Feynman forces govern the forbidden gap,[46] linking the upper valence edge band and the bottom conduction edge band. We term this electronic continuum "the Urbach bridge" that is conceptually illustrated in Figure 3b and the inset of Figure 3a. *The size-dependent closing of the bandgap transforms an amorphous semiconductor into a quasi-metal and enables the observation of indirect and direct optical transitions.*

Within this model, the observed *l*-ERS emission can now be attributed to optical transitions in the vicinity of the Fermi level. Here, we establish a connection between the observed *l*-ERS and emission effects that are associated with photon momentum, phenomena previously reported in rough metals,[32,33] disordered semiconductors,[47] and high entropy oxides.[48] Similar to metals, the *l*-ERS peak remains centered at the Rayleigh line for varying sizes of the crystallites, yet a clear correlation exists between its line width (Γ) and structure size (Figure 3a). An empirical connection between the disorder-driven Raman line width (Γ) and Urbach energy (E_U), i.e., $\Gamma \sim E_U$, has been previously established.[49,50] Our data demonstrates that the *l*-ERS line width (Urbach energy) exhibits an exponential growth that is inversely proportional to the structure size (Figure 3a). At 4 nm, the *l*-ERS line width reaches the value of 43 meV (350 cm^{-1}), while, for larger structures, it asymptotically approaches the thermal energy $kT \approx 23$ meV (200 cm^{-1}). It is crucial to note that the *l*-ERS peak diminishes as the cross-linked glass undergoes excessive or full crystallization.

Applying a similar rationale, the *h*-ERS and its energy redshift are explained as an ERS process linked to an optical transition from the Urbach bridge to the conduction band (Figure 3b). To extract an electron from the trapped state within the bridge in the mobility gap, a change in electron momentum is necessary.[51] While previous studies by Zhang and Drabold[52] have explored the use of phonons to assist in this transition, the authors acknowledge that the energy of a single phonon would not suffice for enabling the transition from deep in the mobility gap as observed by the emission's heavy tail (Figure 2f, >4000 cm^{-1}). Alternatively, both the energy and momentum required for such transitions can be supplied by the photon confined within the nanostructure. Photon localization can occur in disordered media, driven by nanoscale variations in the refractive index. The intricate process can be further improved through the lightning-rod effect[53] in the material, where the distribution of structural size, shape, and asperities—extending down to spatial singularities such as vacancies and sub-to-near nm Si crystallization nuclei—plays a crucial role. These factors should contribute to a significant expansion of photon momentum, enabling indirect optical transitions from deeper states within the Urbach bridge to the conduction band.

To facilitate a careful examination of the data within the context of the proposed Urbach bridge concept, Figure 4 shows Raman spectral maps summarizing the overall trends and correlations observed for two distinct types of structures. The first type, extensively discussed earlier, consists of 1D arrays (Figure 1, Figure 4a−e). The second one comprises a 2D network of cross-linked semiconductor glass (Figure 4f−j). It has been fabricated on a similar a-Si film through scanning the laser beam and forming a network of cross-linked protrusions with a gradually adjusted pitch, as imaged by AFM topography (Figure SF6a). The spectral maps acquired from these structures not only establish clear correlations but affirm a direct connection between structure size, degree of crystallinity, and their corresponding spectral responses.

Parts a,b and f,g of Figure 4 show spectral VRS maps originating from a-Si and c-Si. An inversion of the VRS maps for a-Si and c-Si is evident. Following the discussion above, the degree of crystallinity is intricately tied to the writing speed, driven by a substantial difference in the thermal conductivity between a-Si and c-Si. Hence, in the case of the 1D array, the crystallization in the LAZ and, consequently, the c-Si VRS are depressed when a slower writing speed (0.5 μm/s) is used. At the same time, the boundaries between LAZ and HAZ contain substantial c-Si nanostructures, as confirmed by AFM (Figure 1d), causing these regions to light up in this spectral range. With an increase in writing speed, crystallization proceeds

https://doi.org/10.1021/acsnano.3c12666
ACS Nano 2024, 18, 9557−9565

more uniformly, leading to a decrease in the VRS intensity at the HAZ boundaries.

ERS maps (*l*-ERS and *h*-ERS) for both types of samples follow the spatial distribution of structural sizes and the degree of crystallinity across their surfaces (Figure 4c−e and i,j). To visualize *l*-ERS for the 1D array, we plot the integrated signal at the anti-Stokes wing in the −1200-(−500) cm^{-1} spectral range (Figure 4c), avoiding contributions from other spectral features, particularly the Boson peak. In line with the discussion of data in Figure 3a, the trend shows an increase in the integrated signal (*l*-ERS width, Figure 4c) with a decrease in structure size. Furthermore, a Boson peak map at 140 cm^{-1} for the 2D network is plotted in Figure 4h (see also Figure SF6e). The Boson peak emerges in disordered systems due to the hybridization of plane-wave bulk and confined phonons.[54,55] As can be seen on the spectral map, this peak intensifies with crystallization near the LAZ/HAZ interface due to an increase in v-DOS of bulk phonons, an observation consistent with the VRS maps (Figure 4a,b and f,g) discussed earlier. The Boson peak, however, proves insensitive to thermal impact, as observed in HAZs (Figure SF7), although it shows a slight degradation compared to that of a-Si. This phenomenon may be attributed to thermal-induced amorphization, resulting in increased roughness and stress relaxation.

The *h*-ERS maps, generated by integrating the signals above 600 cm^{-1}, are shown in Figure 4d,e (1D array) and 4i,j (2D network). In the case of the 1D array, the *h*-ERS intensity in LAZ increases with the writing speed. Supporting Information Part VIII provides additional maps generated by integration over a narrower spectral range (Figure SF8). These results corroborate earlier observations detailed in Figure 2c and d—the *h*-ERS energy shift is inversely proportional to the structure size. Following surface topography and the spatial distribution of c-Si nanocrystals, the *h*-ERS extends further away from LAZ and toward HAZ. The *h*-ERS maps of the 2D network exhibit a similar trend (Figure 4i,j). Here, an interesting observation is noted: multiple passes of the laser beam through closely packed spatial locations seem to influence the morphology (or size range) but not the level of crystallinity. This conclusion naturally follows from the direct comparison between the c-Si VRS map (Figure 4g) and the Si glass ERS map (Figure 4i). In areas where multiple laser passes create a smaller pitch (left side of the map, Figure 4i), the intensity of the ERS signal intensifies. The closely packed pitch "foams" the film, causing it to become more heterogeneous by blending amorphous and crystalline phases.

The spectral maps of the ERS heavy tail are presented in Figure 4e and j. Clearly, the *h*-ERS extends beyond the LAZ and the highest energy-shifted ERS signals are observed well into the HAZ. We note that the HAZ is not expected to contain large, fully developed c-Si structures, as preliminary confirmed by c-Si VRS (Figure 4b). However, these areas may host crystal embryos—sub-to-near nm Si crystallization nuclei—which can be present near the LAZ/HAZ interface and extend into the HAZ due to the pressure gradient between the zones.[41] These intriguing subareas can be referred to as pressure-affected zones (PAZs). A photon confined at such crystalline embryos carries both energy and a significantly large momentum, which can be transferred to an electron, facilitating the transition from deep trapped states within the forbidden gap to the conduction band (Figure 3b). This process gives rise to a substantial energy-shifted ERS heavy tail, extending it spectrally well above 4000 cm^{-1} and observable up to 7000 cm^{-1} (Figure SF9). Such energy shifts cannot be explained using conventional electron−phonon interactions.[31,46,56] To demonstrate the effect of pressure driven Si-formations, we conducted a series of experiments using an AFM cantilever (see Supporting Information Part X). In these experiments, the tip was used in the contact tapping mode to create pressure points on an a-Si film. The regions subjected to such pressure exhibit a significant increase in the heavy tail of *h*-ERS, while the spectra show no presence of c-Si (Figure SF10a, orange spot, and corresponding spectrum on Figure SF10c). Furthermore, we observe a clear correlation between the Boson peak and the heavy tail of the ERS response, specifically between the dark inner frames in Figure 4h (Boson peak) and the bright frames in Figure 4j (heavy ERS tail). Interestingly, these regions were not directly affected by laser illumination. Nonetheless, the observed correlation suggests the presence of crystalline embryos formed by local internal stress when the film topology undergoes changes due to laser writing.

CONCLUSIONS

This work presents a detailed study of light emission in heterogeneous cross-linked glass composed of c-Si nanocrystals embedded in an amorphous silicon matrix. With such a model system at hand, we attempt to address a few outstanding questions regarding the origin of PL and discuss the emission spectrum in relation to crystal phase, size, and photon excitation energy. Our findings challenge the conventional notions of phonon-assisted fluorescence in quantum confined systems. To interpret our observations, we revisit the concept proposed in 1970 by Mott and Davis.[28] They suggested that a continuum of energy states forms in the forbidden gap once disorder and crystallinity are presented on the nanoscale. This extended e-DOS establishes a quasi-continuous connection between the conduction and valence bands, here termed an Urbach bridge. We propose that intra- and interband optical transitions within the Urbach bridge underlie the observed emission effect.

The observation and spectral analysis of the *l*-ERS lead us to suggest ERS as the dominant mechanism of emission, a phenomenon previously observed and explained in the context of extended photon momentum on nanoscale asperities of metal surfaces[32] and even individual gold particles.[33] The electronic Raman nature of the emission is further supported by a substantial *h*-ERS redshift, its correlation with size, and lack of dependence on excitation photon energy.

In our proposed model, both emission features originate from the Urbach bridge, a conclusion supported by the synchronous appearance and evolution of the signals upon mixing of amorphous and crystalline phases. Both features disappear when the system is fully transformed to bulk c-Si. The *l*-ERS on the Urbach bridge is associated with ERS transitions near the Fermi level. We argue that confined photons with expanded momentum likely exist in a nanostructured a-Si/c-Si matrix. Interband optical transitions from the Urbach bridge to the conduction band are responsible for *h*-ERS. This insight helps explain its heavy tail (>4000 cm^{-1} energy shift, see Figure SF9a and b) originating from transitions between deep states in the forbidden gap and the conduction band. These transitions require the smallest structural confinement and a large photon momentum available at embryonic c-Si sites. The size dependence of the *l*-ERS and *h*-ERS underscores their potential utility as

https://doi.org/10.1021/acsnano.3c12666
ACS Nano 2024, 18, 9557−9565

spectroscopic probes for quantifying the structural disorder in vitreous semiconductors and empowers optical spectroscopy to enable structural analysis of disordered solids. Our findings hold significant promise in the realm of semiconductor photonics, encompassing applications in the areas of solar energy conversion, light emitting diodes, optical sensors, and lasers.

Lastly, we highlight an apparent similarity between the ERS and Compton scattering processes. The Compton effect occurs when a propagating photon with a relatively large momentum, i.e., X-ray, scatters upon an electron.[57] Similarly, the ERS phenomenon discussed here is driven by a confined visible photon with enhanced momentum that interacts with an electron in a trapped state within the forbidden energy gap. The matching of electron and photon momenta enables these light−matter interactions that are otherwise forbidden. While one of the conventional and efficient methods to confine light involves utilizing plasmon resonances, its efficacy diminishes when the structure size is less than 5 nm. Our work suggests that the involvement of photons confined to crystalline nanostructures within the heterogeneous glass can overcome the momentum requirement for the observed ERS transitions, underlining the relevance of such photonic states in the optical response of disordered materials.

METHODS/EXPERIMENTAL

Sample Preparation. A modified Gatan Precision Ion Polishing System (PIPS, Gatan Inc.) was used as a sputter coater for a-Si thin film deposition on the borosilicate microscopy coverslip (170 μm). A modification of the PIPS enables coating of bulk sample surfaces and the deposition of thin films of a variety of materials. An advantage of using PIPS for the latter purpose is the oil-free vacuum system, which allows films to be deposited with minimal carbon contamination. The sputter source was a piece of monocrystal wafer about 5 mm in diameter mounted on a standard specimen holder post. This milling system consists of two rare-earth Penning-type ion guns (PIGs), which were used together to accelerate the sputtering process. The angle between guns and rotating target source material was +150° and did not change during the process. The system operated at the maximum acceleration voltage of 8 kV. The wafer source was sputter-cleaned for 2 min (pneumatic shutter in closed position) before the deposition process started. The vacuum level prior to deposition was typically 10^{-3} Pa or better. Typical sputtering times for producing amorphous thin films were in the range of 30 to 90 min, depending on the sputter source and thickness required.

Atomic Force Microscopy. The multimode scanning probe microscope Prima (NT-MDT) was utilized for visualizing the topography of the light-structured silicon glass samples. The AFM cantilever (VIT_P) was made of antimony-doped single crystal silicon (n-type, 0.01−0.025 Ohm-cm). The tip height was 14−16 μm, the tip curvature radius was 30 nm, and the resonance frequency was 300 kHz. For the height analysis, a 67% confidence (3σ) interval was used in Figure 1e and f (full range over heights).

Raman Spectroscopy and Microscopy. Raman spectra and maps were captured with a multipurpose analytical instrument NTEGRA SPECTRA (NT-MDT) in the upright configuration. The confocal spectrometer was wavelength calibrated with a crystalline silicon (100) wafer by registering the first-order Raman band at 521 cm^{-1}. A sensitivity of the spectrometer was as high as ca. 1700 photon counts per 0.1 s when a 100× objective (N.A. = 0.7) was used, along with an exit slit (pinhole) of 100 μm and linearly polarized light with a wavelength of 632.8 nm. The illumination power of the sample was 10 mW. A Newton EMCCD camera (ANDOR) was employed without using the amplification option. Low-frequency Raman measurements were performed using a 633 nm Bragg notch filter (OptiGrate) with a spectral blocking window of 10 cm^{-1}. For spectral intensity analysis, a 95% confidence interval (2σ) was used, averaged over 10 points.

ASSOCIATED CONTENT

Supporting Information

The Supporting Information is available free of charge at https://pubs.acs.org/doi/10.1021/acsnano.3c12666.

Additional discussions on light-assisted structuring of a-Si, the electron thermalization model, the effect of quantum confinement on the c-Si bandgap, emission from light and heat affected zones of cross-linked glass, and the confined photon density of states; Raman spectra of the Boson peak and its structural dependence; and additional Raman images of the light-structured metasurface across a broad spectral range, including the heavy tail spectral region (PDF)

AUTHOR INFORMATION

Corresponding Authors

Sergey S. Kharintsev − *Department of Optics and Nanophotonics, Institute of Physics, Kazan Federal University, Kazan 420008, Russia;* orcid.org/0000-0002-5788-3401; Email: skharint@gmail.com

Dmitry A. Fishman − *Department of Chemistry, University of California Irvine, Irvine, California 92697, United States;* orcid.org/0000-0001-6287-2128; Email: dmitryf@uci.edu

Authors

Elina I. Battalova − *Department of Optics and Nanophotonics, Institute of Physics, Kazan Federal University, Kazan 420008, Russia*

Aleksey I. Noskov − *Department of Optics and Nanophotonics, Institute of Physics, Kazan Federal University, Kazan 420008, Russia; Department of Chemistry, University of California Irvine, Irvine, California 92697, United States*

Jovany Merham − *Department of Chemistry, University of California Irvine, Irvine, California 92697, United States;* orcid.org/0000-0003-3151-1877

Eric O. Potma − *Department of Chemistry, University of California Irvine, Irvine, California 92697, United States;* orcid.org/0000-0003-3916-6131

Complete contact information is available at: https://pubs.acs.org/10.1021/acsnano.3c12666

Notes

The authors declare no competing financial interest.

ACKNOWLEDGMENTS

D.A.F. and S.S.Kh. would like to thank Yulia Davydova and Natalia Bratkova for help and support. The authors thank Prof. Alexander Fishman, Prof. Sasha Chernyshev, and Prof. Maxx Arguilla for the fruitful discussions. S.S.Kh. acknowledges RSF Grant No. 19-12-00066-P for experimental studies of cross-linked heterogeneous silicon glass. E.I.B. acknowledges support from the subsidy allocated to Kazan Federal University for the state assignment in the sphere of scientific activities (FZSM-2022-0021) for numerical decomposition of composite Raman spectra. A CVD synthesis of a-Si thin films was supported by the Kazan Federal University Strategic Academic Leadership Program (PRIORITY-2030). D.A.F. and E.O.P. are thankful to the Chan-Zuckerberg Initiative and grant 2023-321174 (5022) GB-1585590 for developing a theoretical model of light

emission in silicon glass. All authors acknowledge technical support from NT-MDT BV (The Netherlands).

REFERENCES

(1) Pavesi, L. Thirty Years in Silicon Photonics: A Personal View. *Front. Phys.* **2021**, *9*, No. 786028.
(2) Liang, D.; Bowers, J. E. Recent Progress in Lasers on Silicon. *Nat. Photonics* **2010**, *4*, 511−517.
(3) Cao, W.; Bu, H.; Vinet, M.; Cao, M.; Takagi, S.; Hwang, S.; Ghani, T.; Banerjee, K. The Future Transistors. *Nature* **2023**, *620*, 501−515.
(4) Canham, L. *Handbook of Porous Silicon*; Springer: New York, 2014.
(5) Gelloz, B. Photoluminescence of Porous Silicon. In *Handbook of Porous Silicon*; Canham, L., Ed.; Springer: New York, 2014; pp 307−320.
(6) Pavesi, L.; Ceschini, M.; Rossi, F. Photoluminescence of Porous Silicon. *J. Lumin.* **1993**, *57*, 131−135.
(7) Qin, G. G.; Jia, Y. Q. Mechanism of the Visible Luminescence in Porous Silicon. *Solid State Commun.* **1993**, *86*, 559−563.
(8) Andersen, O. K.; Veje, E. Experimental Study of the Energy-Band Structure of Porous Silicon. *Phys. Rev. B* **1996**, *53*, 15643−15652.
(9) Bayliss, S.; Zhang, Q.; Harris, P. Network Dimensionality of Porous Si and Ge. *Appl. Surf. Sci.* **1996**, *102*, 390−394.
(10) Wolkin, M. V.; Jorne, J.; Fauchet, P. M.; Allan, G.; Delerue, C. Electronic States and Luminescence in Porous Silicon Quantum Dots: The Role of Oxygen. *Phys. Rev. Lett.* **1999**, *82*, 197−200.
(11) Canham, L. Introductory Lecture: Origins and Applications of Efficient Visible Photoluminescence from Silicon-Based Nanostructures. *Faraday Discuss.* **2020**, *222*, 10−81.
(12) Guha, S.; Steiner, P.; Kozlowski, F.; Lang, W. Investigation of Porous Si Grains by Optical Spectroscopy. *Thin Solid Films* **1995**, *255*, 119−122.
(13) Delerue, C.; Allan, G.; Lannoo, M. Theoretical Aspects of the Luminescence of Porous Silicon. *Phys. Rev. B* **1993**, *48*, 11024−11036.
(14) Delley, B.; Steigmeier, E. F. Quantum Confinement in Si Nanocrystals. *Phys. Rev. B* **1993**, *47*, 1397−1400.
(15) Koch, F.; Petrova-Koch, V.; Muschik, T.; Nikolov, A.; Gavrilenko, V. Some Perspectives on the Luminescence Mechanism via Surface-Confined States of Porous Si. *Mater. Res. Soc. Symp. Proc.* **1992**, *283*, 197−202.
(16) Prokes, S. M.; Glembocki, O. J.; Bermudez, V. M.; Kaplan, R.; Friedersdorf, L. E.; Searson, P. C. SiH_x Excitation: An Alternate Mechanism for Porous Si Photoluminescence. *Phys. Rev. B* **1992**, *45*, 13788−13791.
(17) Brandt, M. S.; Fuehs, H. D.; Stutzmann, M.; Weber, J.; Cardona, M. The Origin of Visible Luminescence from "Porous Silicon": A New Interpretation. *Solid State Commun.* **1992**, *81*, 307−312.
(18) Vial, J. C.; Bsiesy, A.; Gaspard, F.; Hérino, R.; Ligeon, M.; Muller, F.; Romestain, R.; Macfarlane, R. M. Mechanisms of Visible-Light Emission from Electro-Oxidized Porous Silicon. *Phys. Rev. B* **1992**, *45*, 14171−14176.
(19) Bharadwaj, P.; Deutsch, B.; Novotny, L. Optical Antennas. *Adv. Opt. Photonics* **2009**, *1*, 438−483.
(20) Agio, M.; Alu, A. *Optical Antennas*; Cambridge University Press: New York, 2013.
(21) Rama Krishna, M. V.; Friesner, R. A. Prediction of Anomalous Redshift in Semiconductor Clusters. *J. Chem. Phys.* **1992**, *96*, 873−877.
(22) de Boer, W. D. A. M.; Timmerman, D.; Dohnalova, K.; Yassievich, I. N.; Zhang, H.; Buma, W. J.; Gregorkiewicz, T. Red Spectral Shift and Enhanced Quantum Efficiency in Phonon-Free Photoluminescence from Silicon Nanocrystals. *Nat. Nanotechnol.* **2010**, *5*, 878−884.
(23) Baffou, G. Anti-Stokes Thermometry in Nanoplasmonics. *ACS Nano* **2021**, *15*, 5785−5792.
(24) Inagaki, M.; Isogai, T.; Motobayashi, K.; Lin, K.-Q.; Ren, B.; Ikeda, K. Electronic and Vibrational Surface-Enhanced Raman Scattering: From Atomically Defined Au(111) and (100) to Roughened Au. *Chem. Sci.* **2020**, *11*, 9807−9817.
(25) Fluegel, B.; Mialitsin, A. V.; Beaton, D. A.; Reno, J. L.; Mascarenhas, A. Electronic Raman Scattering as an Ultra-Sensitive Probe of Strain Effects in Semiconductors. *Nat. Commun.* **2015**, *6*, 7136.
(26) Ismailov, T. G.; Nazanly, R. A. Interband Electronic Raman Scattering in Semiconductors Induced by Nonparabolicity. *Phys. Status Solidi* **1991**, *164*, 553−560.
(27) Shukla, A. K.; Kumar, R.; Kumar, V. Electronic Raman Scattering in the Laser-Etched Silicon Nanostructures. *J. Appl. Phys.* **2010**, *107*, No. 014306.
(28) Davis, E. A.; Mott, N. F. Conduction in Non-Crystalline Systems V. Conductivity, Optical Absorption and Photoconductivity in Amorphous Semiconductors. *Philos. Mag.* **1970**, *22*, 0903−0922.
(29) Ibrahim, A.; Al-Ani, S. K. J. Models of Optical Absorption in Amorphous Semiconductors at the Absorption Edge − A Review and Re-Evaluation. *Czech. J. Phys.* **1994**, *44*, 785−797.
(30) Cai, W. R.; Mei, J. J.; Shen, W. Z. A Proposal for Complete Interband Absorption in Indirect Semiconductors. *Phys. B* **2004**, *352*, 179−184.
(31) Kharintsev, S. S.; Noskov, A. I.; Battalova, E. I.; et al. Photon Momentum Enabled Light Absorption in Silicon. 2023, arXiv 2304.14521, https://arxiv.org/abs/2304.14521 (accessed November 21, 2023).
(32) Shalaev, V. M.; Douketis, C.; Haslett, T.; Stuckless, T.; Moskovits, M. Two-Photon Electron Emission from Smooth and Rough Metal Films in the Threshold Region. *Phys. Rev. B* **1996**, *53*, 11193−11206.
(33) Beversluis, M.; Bouhelier, A.; Novotny, L. Continuum Generation from Single Gold Nanostructures through Near-Field Mediated Intraband Transitions. *Phys. Rev. B* **2003**, *68*, No. 115433.
(34) Rivera, N.; Kaminer, I.; Zhen, B.; Joannopoulos, J. D.; Soljačić, M. Shrinking Light to Allow Forbidden Transitions on the Atomic Scale. *Science* **2016**, *353*, 263−269.
(35) Mott, N. F.; Davis, E. A.; Street, R. A. States in the Gap and Recombination in Amorphous Semiconductors. *Philos. Mag.* **1975**, *32*, 961−996.
(36) Drabold, D. A.; Li, Y.; Cai, B.; Zhang, M. Urbach Tails of Amorphous Silicon. *Phys. Rev. B* **2011**, *83*, No. 045201.
(37) Pierce, D. T.; Spicer, W. E. Electronic Structure of Amorphous Si from Photoemission and Optical Studies. *Phys. Rev. B* **1972**, *5*, 3017−3029.
(38) Wada, H.; Kamijoh, T. Thermal Conductivity of Amorphous Silicon. *Jpn. J. Appl. Phys.* **1996**, *35*, L648−L650.
(39) Thutupalli, G. K. M.; Tomlin, S. G. The Optical Properties of Amorphous and Crystalline Silicon. *J. Phys. C: Solid State Phys.* **1977**, *10*, 467−477.
(40) Paesler, M. A.; Sayers, D. E.; Tsu, R.; Gonzalez-Hernandez, J. Ordering of Amorphous Germanium Prior to Crystallization. *Phys. Rev. B* **1983**, *28*, 4550−4557.
(41) Spinella, C.; Lombardo, S.; Priolo, F. Crystal Grain Nucleation in Amorphous Silicon. *J. Appl. Phys.* **1998**, *84*, 5383−5414.
(42) Parker, J. H.; Feldman, D. W.; Ashkin, M. Raman Scattering by Silicon and Germanium. *Phys. Rev.* **1967**, *155*, 712−714.
(43) Kim, H.; Park, G.; Park, S.; Kim, W. Strategies for Manipulating Phonon Transport in Solids. *ACS Nano* **2021**, *15*, 2182−2196.
(44) Ching, W. Y.; Lin, C. C.; Huber, D. L. Electronic Energy Structure of Amorphous Silicon. *Phys. Rev. B* **1976**, *14*, 620−631.
(45) Kramer, B. Electronic Structure and Optical Properties of Amorphous Germanium and Silicon. *Phys. Status Solidi* **1971**, *47*, 501−510.
(46) Prasai, K.; Biswas, P.; Drabold, D. A. Electrons and Phonons in Amorphous Semiconductors. *Semicond. Sci. Technol.* **2016**, *31*, No. 073002.
(47) Yaffe, O.; Guo, Y.; Tan, L. Z.; Egger, D. A.; Hull, T.; Stoumpos, C. C.; Zheng, F.; Heinz, T. F.; Kronik, L.; Kanatzidis, M. G.; Owen, J.

https://doi.org/10.1021/acsnano.3c12666
ACS Nano 2024, 18, 9557−9565

S.; Rappe, A. M.; Pimenta, M. A.; Brus, L. E. Local Polar Fluctuations in Lead Halide Perovskite Crystals. *Phys. Rev. Lett.* **2017**, *118*, No. 136001.
(48) Oses, C.; Toher, C.; Curtarolo, S. High-Entropy Ceramics. *Nat. Rev. Mater.* **2020**, *5*, 295−309.
(49) Rambadey, O. V.; Kumar, A.; Kumar, K.; Mishra, V.; Sagdeo, P. R. Methodology to Probe Disorder Contribution in Raman Linewidth via Optical Absorption Spectroscopy in Orthoferrite $EuFeO_3$. *J. Phys. Chem. C* **2022**, *126*, 13946−13956.
(50) Rambadey, O. V.; Gupta, M.; Kumar, A.; Sagdeo, P. R. Analysis of Structural Disorder on Raman Spectra of Semiconductors. *J. Appl. Phys.* **2023**, *133*, No. 131101.
(51) Frohlich, H. Energy Distribution and Stability of Electrons in Electric Fields. *Proc. R. Soc. A* **1947**, *188*, 532−541.
(52) Zhang, M.-L.; Drabold, D. A. Phonon Driven Transport in Amorphous Semiconductors: Transition Probabilities. *Eur. Phys. J. B* **2010**, *77*, 7−23.
(53) Anderson, N.; Bouhelier, A.; Novotny, L. Near-Field Photonics: Tip-Enhanced Microscopy and Spectroscopy on the Nanoscale. *J. Opt. A: Pure Appl. Opt.* **2006**, *8*, S227−S233.
(54) Ovsyuk, N. N.; Novikov, V. N. Influence of Structural Disorder on Raman Scattering in Amorphous Porous Silicon. *Phys. Rev. B* **1998**, *57*, 14615−14618.
(55) Hu, Y.-C.; Tanaka, H. Origin of the Boson Peak in Amorphous Solids. *Nat. Phys.* **2022**, *18*, 669−677.
(56) Yamada, Y.; Kanemitsu, Y. Electron-Phonon Interactions in Halide Perovskites. *NPG Asia Mater.* **2022**, *14*, 48.
(57) Compton, A. H. Quantum Theory of the Scattering of X-rays by Light Elements. *Phys. Rev.* **1923**, *21*, 483−502.

https://doi.org/10.1021/acsnano.3c12666
ACS Nano 2024, 18, 9557−9565